Automated Segmentation of Optic Nerve Head Structures With Optical Coherence Tomography

Faisal A. Almobarak,[1,2] Neil O'Leary,[1,3] Alexandre S. C. Reis,[1,4] Glen P. Sharpe,[1] Donna M. Hutchison,[1] Marcelo T. Nicolela,[1] and Balwantray C. Chauhan[1]

[1]Department of Ophthalmology and Visual Sciences, Dalhousie University, Halifax, Nova Scotia, Canada
[2]Department of Ophthalmology, College of Medicine, King Saud University, Riyadh, Saudi Arabia
[3]Centre for Biostatistics, Institute of Population Health, School of Medicine, University of Manchester, Manchester, United Kingdom
[4]Department of Ophthalmology, University of São Paulo, São Paulo, Brazil

Correspondence: Balwantray C. Chauhan, Department of Ophthalmology and Visual Sciences, Dalhousie University, 1276 South Park Street, 2W Victoria, Halifax, Nova Scotia, Canada B3H 2Y9; bal@dal.ca.

Submitted: September 21, 2013
Accepted: January 14, 2014

Citation: Almobarak FA, O'Leary N, Reis ASC, et al. Automated segmentation of optic nerve head structures with optical coherence tomography. *Invest Ophthalmol Vis Sci*. 2014;55:1161–1168. DOI:10.1167/iovs.13-13310

Purpose. To quantify and characterize the difference between automated and manual segmentation of optic nerve head structures with spectral-domain optical coherence tomography (SD-OCT).

Methods. Optic nerve head radial scans in 107 glaucoma patients and 48 healthy controls were conducted with SD-OCT. Independent segmentations of the internal limiting membrane (ILM) and Bruch's membrane opening (BMO) were performed manually with custom software and with an automated algorithm in each radial scan. The minimum distance between BMO and ILM, termed BMO–minimum rim width (BMO-MRW) was calculated with each segmentation method. Absolute differences between automated and manual segmentations of ILM (ΔILM) and BMO (ΔBMO), and the resulting computation of BMO-MRW (ΔBMO-MRW) were computed. Finally, the relationship between image quality score and ΔILM and ΔBMO was explored.

Results. The median (interquartile range, IQR) ΔILM was 8.9 (6.5, 13.4) μm in patients and 7.3 (5.3, 9.9) μm in controls. The corresponding values for ΔBMO were 11.5 (6.6, 22.1) μm and 12.4 (6.8, 25.4) μm. Subject-averaged ΔILM was higher in patients than controls ($P < 0.01$); however, mean ΔBMO was not ($P = 0.09$). The median (IQR) subject-averaged absolute ΔBMO-MRW was 13.4 (10.6, 16.8) μm in patients and 12.1 (10.0, 16.8) μm in controls and not statistically different ($P = 0.21$). Mean image quality score was statistically higher in controls than patients ($P = 0.03$) but not related to subject-averaged ΔILM or ΔBMO.

Conclusions. In individual scans, the median difference in ILM and BMO segmentations was <2 and <3 image pixels, respectively. There were no differences between patients and controls in ΔBMO-MRW.

Keywords: glaucoma, optic nerve head, optical coherence tomography

Spectral-domain optical coherence tomography (SD-OCT) enables visualization of key structures in the retina and optic nerve head (ONH),[1–3] previously not possible with existing clinical techniques. Traditional quantification of the neuroretinal rim with clinical, photographic, or confocal scanning laser tomographic techniques relies on identifying the outermost and innermost borders of the rim, respectively the clinically visible optic disc margin and the optic cup.[4] Recent research with SD-OCT has indicated that the clinically visible disc margin is not a consistent or accurate anatomic landmark from which rim estimates can be reliably made.[5,6] Conventionally, the optic cup is either estimated clinically by the subjective appearance of the ONH surface, or with imaging devices as the portion of the enclosed disc area that lies beneath an arbitrary reference plane.[7–9] Hence, neither the optic disc nor cup margins by these definitions appear to be anatomically defensible structures.

Several investigators have proposed that Bruch's membrane opening (BMO) represents a consistent anatomic border that can serve as a reference point from which rim parameters of the ONH can be computed.[5,10–13] Rim width quantification requires identification, hereafter referred to as segmentation, of BMO and the internal limiting membrane (ILM), respectively the outermost and innermost boundary of the rim. To account for the varying trajectory of the retinal nerve fiber bundles at BMO, it has been proposed that the minimum distance from BMO to the ILM represents a geometrically accurate estimate of rim width.[5,11–13] This index, termed BMO–minimum rim width (BMO-MRW),[5] has clinical value as it discriminates glaucoma patients from healthy controls subjects with more accuracy than current methods of quantifying the rim with confocal scanning laser tomography or SD-OCT.[14]

Various SD-OCT–based studies have relied on manual segmentation of ONH structures.[5,14,15] For computation of rim width, the operator is required to segment BMO and the ILM in multiple B-scans from SD-OCT in a single eye, a time-consuming process that is impractical for routine clinical use.

Automated segmentation of the ILM and Bruch's membrane, including BMO,[10,16] is currently used in commercial SD-OCT devices.[17,18] To date, published studies have been limited to reporting the agreement between manual and automated segmentation methods primarily for deriving traditional indices

Table 1. Summary of Data From Individual B-Scans*

	Glaucoma	Control	All Subjects
Image quality score, dB	26.6 (23.3, 30.8)	28.2 (25.6, 30.7)	27.2 (24.0, 30.7)
ΔILM, μm	8.9 (6.5, 13.4)	7.3 (5.3, 9.9)	8.3 (6.1, 12.2)
ΔILM inside BMO, μm	12.9 (8.5, 25.2)	10.0 (7.1, 17.6)	11.8 (7.9, 22.8)
ΔILM outside BMO, μm	5.3 (4.0, 7.2)	4.5 (3.4, 6.2)	5.0 (3.8, 6.9)
ΔBMO, μm	11.5 (6.6, 22.1)	12.4 (6.8, 25.4)	11.7 (6.7, 23.0)
Absolute ΔBMO-MRW, μm	9.4 (4.2, 18.2)	7.9 (3.7, 15.9)	8.9 (4.0, 17.5)
Absolute ΔBMO-MRW, %	5.4 (2.3, 11.5)	2.6 (1.2, 5.5)	4.3 (1.8, 9.4)
Signed ΔBMO-MRW, μm	−2.4 (−10.8, 7.1)	−2.9 (−9.6, 5.0)	−2.6 (−10.4, 6.3)
Signed ΔBMO-MRW, %	−1.4 (−6.2, 4.2)	−1.0 (−3.2, 1.6)	−1.2 (−5.1, 3.1)

* Values shown are median (interquartile range).

such as cup-disc ratio and rim area,[10,16,19,20] with the assumption that BMO represents the disc margin. The aim of our study was to quantify and characterize the differences between an automated segmentation algorithm and manual methods to identify the ILM and BMO. We evaluated how the derived parameter BMO-MRW differed between these segmentation methods.

Methods

Participants

Participants included patients with open-angle glaucoma and healthy normal controls. They were recruited from longitudinal studies at the Eye Care Centre, Queen Elizabeth II (QE-II) Health Sciences Centre, Halifax, Nova Scotia, Canada. The study adhered to the tenets of the Declaration of Helsinki, and all subjects gave written, informed consent. If both eyes were eligible, one eye was randomly selected as the study eye. The study was approved by the Research Ethics Board of the QE-II Health Sciences Centre.

For patients, inclusion criteria were (1) clinical diagnosis of open-angle glaucoma, including primary, pseudo-exfoliative, or pigmentary glaucoma; (2) clinically judged glaucomatous ONH changes with stereo disc photography or confocal scanning laser tomography; (3) a positive Glaucoma Hemifield Test with standard automated perimetry (Swedish Interactive Thresholding Algorithm program 24-2 of the Humphrey Field Analyzer; Carl Zeiss Meditec, Dublin, CA); and (4) best corrected visual acuity equal to or better than 0.3-logarithm minimum angle of resolution (equivalent to 20/40). Exclusion criteria were (1) concomitant ocular disease and systemic medication known to affect the visual field and (2) refractive error exceeding ±6.00 diopters (D) sphere or ±3.00 D astigmatism.

For healthy controls, inclusion criteria were (1) normal eye examination with intraocular pressure less than 21 mm Hg; and (2) normal visual field defined as a Glaucoma Hemifield Test, mean deviation and pattern standard deviation within normal limits. The exclusion criterion was refractive error exceeding ±6.00 D sphere or ±3.00 D astigmatism.

Imaging

The ONH was imaged with SD-OCT (Spectralis; Heidelberg Engineering GmbH, Heidelberg, Germany) with a radial scanning pattern centered on the ONH to obtain 24 angularly equidistant radial B-scans. Each radial B-scan was averaged from 30 individual scans with 768 A-scans per B-scan. The internal image registration and tracking software was used to significantly reduce the effects of eye movements.[21]

Segmentation of ONH Structures

The SD-OCT raw data were imported into customized software, based on the Visualization Toolkit (VTK, Clifton Park, NY), enabling three-dimensional visualization and manual segmentation of BMO and the ILM. The positions of the ILM and BMO (two per B-scan) were manually segmented in each of the 24 radial B-scans by one trained observer (FAA).

An automated segmentation algorithm (Heidelberg Eye Explorer 5.7.0.9; Heidelberg Engineering) automatically segmented BMO and the ILM. The manual and automated segmentations were performed independently and were not mutually informative.

The three-dimensional coordinates of these structures were then used to calculate BMO-MRW, representing the minimum distance between the BMO and ILM with segmentation method.

Analyses

The absolute difference in depth between the automated and manual segmentation of the ILM (ΔILM) was computed for each pixel along each B-scan and averaged for values inside and outside BMO (as determined by the manual method), as well as for the entire B-scan, yielding one value respectively per B-scan. The distance between the automated and manual segmentation of each BMO position (absolute difference, ΔBMO) was then computed, yielding two values per B-scan. Finally, the absolute (representing bias and variability) and signed (representing bias) difference in BMO-MRW (automated–manual, ΔBMO-MRW) derived from the two segmentation methods was computed, each yielding two values per B-scan.

To determine whether the magnitude of BMO-MRW was associated with ΔBMO-MRW, the latter was examined as a function of BMO-MRW derived from the manual method. The variation of ΔBMO with respect to regional position was investigated by plotting ΔBMO as a function of the angle of BMO around the BMO center (computed from a spline fit of the manual BMO segmentation points). These data were averaged according to the nonparametric Friedman supersmoother spline fitting function.[22] These analyses were repeated with the absolute and signed ΔBMO-MRW. The final analyses on individual B-scans examined the association between image quality score (based on signal to noise ratio and ranging from 0 to 40, with higher values indicating higher image quality) and both ΔILM and ΔBMO.

Differences between automated and manual parameters were averaged across all scans for each subject, that is, subject-averaged ΔILM, ΔBMO, and absolute and signed ΔBMO-MRW (derived from the 48 individual absolute and signed ΔBMO-MRW values, respectively). The association among these variables was assessed, as well as that between mean image quality score and both subject-averaged ΔILM and ΔBMO.

Investigative Ophthalmology & Visual Science

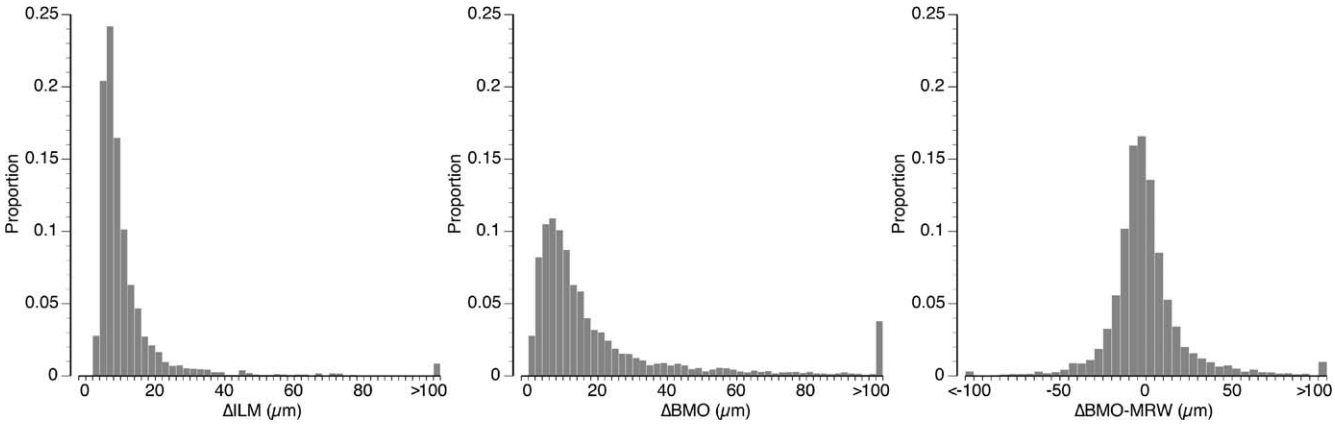

Figure 1. Distribution of the absolute difference between the automated and manual segmentation of the internal limiting membrane (ΔILM, *left*) and Bruch's membrane opening (ΔBMO, *center*) in individual B-scans. Distribution of the signed (automated–manual) difference in BMO-MRW (ΔBMO-MRW, *right*) derived from the two segmentation methods.

Failure of the automated segmentation algorithm to segment either of the two BMO positions in a single B-scan was termed a segmentation failure. In these scans, it was not possible to derive BMO-MRW with the automated algorithm and hence also not ΔBMO-MRW. The segmentation failure rate was defined as the number of segmentation failures per subject. The association between segmentation failure rate and mean image quality score was also assessed.

Group variables were compared with the Mann-Whitney *U* test. Associations between variables were examined with Spearman's rank correlation.

Results

The study population comprised 107 patients with glaucoma and 48 healthy controls. The median (interquartile range, IQR) age and visual field mean deviation was 70.3 (64.3, 76.9) years and 65.0 (58.1, 73.9) years, and −3.92 (−7.87, −1.62) dB and 0.33 (−0.32, 0.98) dB, respectively.

Image quality score, ΔILM, ΔBMO, and ΔBMO-MRW statistics are shown in Table 1. The median ΔILM and ΔBMO was approximately 8 μm and 12 μm, respectively; however, the distributions had long positive tails (Fig. 1). The distribution of signed ΔBMO-MRW had a peak close to 0 μm, but also had long tails containing a small number of observations (Fig. 1). The regional variation of ΔBMO in individual B-scans is shown in Figure 2. Except around the superior pole, in both glaucoma patients and controls, there were no discernible variations in ΔBMO with angular position around the BMO center, with the regional mean ranging from 19.3 to 24.8 μm (Fig. 2). For both patients and controls, there was negligible bias in ΔBMO-MRW (values close to 0 μm, Fig. 3). Furthermore, there was no change in bias as a function of BMO-MRW, with the latter explaining only 0.3% of the variability of signed ΔBMO-MRW (Fig. 3). There were also no discernable variations in the absolute or signed BMO-MRW with angular position around the BMO center (Supplementary Fig. S1); however, absolute ΔBMO-MRW tended to be marginally higher in patients superotemporally and nasally through inferiorly.

For individual B-scans, neither ΔILM nor ΔBMO were associated with image quality score (Spearman's $\rho = 0.06$ and −0.02, respectively; Fig. 4). The subject-averaged image quality score was statistically significantly higher in controls than patients, while all three of the subject-averaged ΔILM parameters higher in patients than controls (Table 2). In both patients and controls, the difference between ΔILM inside

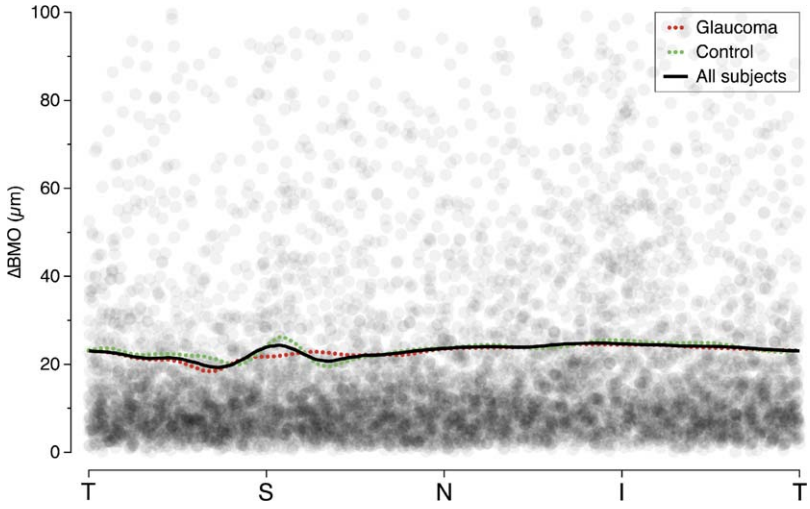

Figure 2. Absolute difference between the automated and manual segmentation of Bruch's membrane opening (ΔBMO) in individual B-scans as a function of the angle around BMO center. *Lines* in the plot indicate the mean values in glaucoma patients, controls, and all subjects fitted with the Friedman supersmoother function. T, temporal; S, superior; N, nasal; I, inferior.

Investigative Ophthalmology & Visual Science

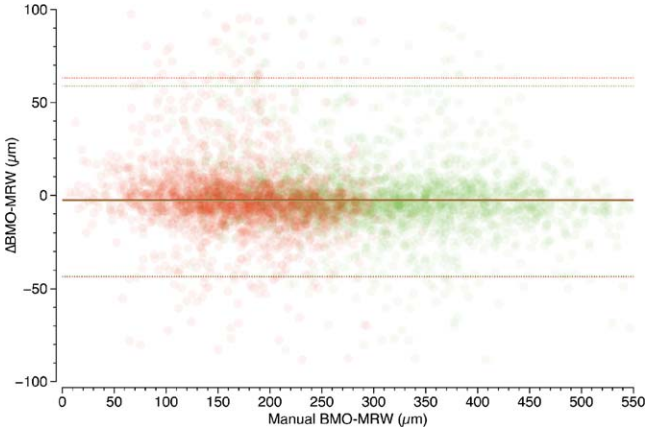

FIGURE 3. Signed (automated–manual) difference in BMO-MRW (ΔBMO-MRW) derived from the two segmentation methods as a function of the BMO-MRW derived from manual segmentation. *Red data points*: Glaucoma patients. *Green data points*: Controls. *Solid red* and *green lines*: Median value in patients and controls, respectively. *Dotted lines*: 2.5th and 97.5th percentiles.

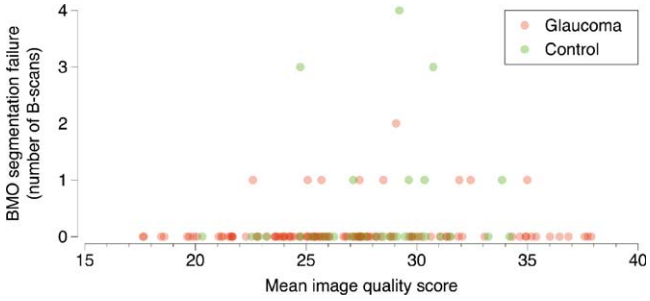

FIGURE 5. Bruch's membrane opening segmentation failure rate, the number of B-scans per subject where neither BMO positions were segmented by the automated algorithm, as a function of subject-averaged image quality score.

BMO was almost three times higher than that outside BMO (Table 2). There was no evidence for differences between patients and controls in subject-averaged absolute or signed ΔBMO-MRW (Table 2); however, because glaucoma patients had thinner BMO-MRW, ΔBMO-MRW, expressed as percentage, was higher in patients than controls (Table 2). There was no difference in bias of global BMO-MRW measurements between patients and controls (Table 2). Absolute subject-averaged ΔBMO-MRW was statistically correlated with subject-averaged ΔILM ($\rho = 0.39$, $P < 0.01$; Supplementary Fig. S2) and ΔBMO ($\rho = 0.53$, $P < 0.01$; Supplementary Fig. S2). Neither subject-averaged ΔILM nor ΔBMO were associated with mean image quality score ($\rho = 0.12$, $P = 0.15$ and $\rho = -0.10$, $P = 0.20$, respectively; Supplementary Fig. S3). Subject-averaged ΔBMO-MRW was not associated with visual field mean deviation in either patients ($\rho = -0.06$, $P = 0.58$), or all subjects taken together ($\rho = -0.12$, $P = 0.12$).

Subject-averaged BMO-MRW estimated with manual segmentation was significantly lower in patients than controls ($P < 0.01$) with a median difference (95% confidence interval) of 127.2 (108.8, 146.6) μm. The 95% prediction interval of subject-averaged absolute ΔBMO-MRW was 6.6 to 37.7 μm. Thus, the upper limit of this 95% prediction interval of absolute ΔBMO-MRW (37.7 μm) was less than the lower limit of the 95% confidence interval of the difference in median BMO-MRW between glaucoma patients and controls (108.8 μm). In other words, 95% of all differences in BMO-MRW would be, at most, approximately 3 times smaller than a conservative estimate for the size of BMO-MRW difference between the average glaucoma patient and control subject.

The automated segmentation failure rate (the number of B-scans where neither of the two BMO positions was segmented) ranged from 0 to 4 (Fig. 5). In 139 (90.3%) subjects, of whom 98 (91.6%) were patients and 41 (85.4%) were controls, the failure rate was 0. In 12 (7.8%) subjects (8 [7.5%] patients and 4 [8.3%] controls), the failure rate was 1; in 1 (0.6%) subject (1 [0.9%] patient), it was 2; in 2 (1.3%) subjects (2 [4.2%] controls), it was 3; and in 1 (0.6%) subject (1 [2.1%] control), it was 4. In all but one case, segmentation failure occurred where the ILM was not fully segmented, typically when excavation of the ONH was profound and the instrument scan depth was incapable of capturing the anterior surface of prelaminar tissue and the entire ILM. Hence, in these cases, ΔILM, ΔBMO, or ΔBMO-MRW could not be computed. There was a poor relationship between segmentation failure rate and mean image quality score ($\rho = 0.14$, $P = 0.08$; Fig. 5).

Figure 6 (A and B) depicts two cases illustrating that image quality was not a good predictor of the agreement between the automated and manual segmentation methods (i.e., ΔILM and ΔBMO, and ΔBMO-MRW derived from the two methods). Figure 7 depicts infrequent but meaningful differences between the two methods, one case (Fig. 7A) due to automated segmentation of BMO at externally oblique border tissues and

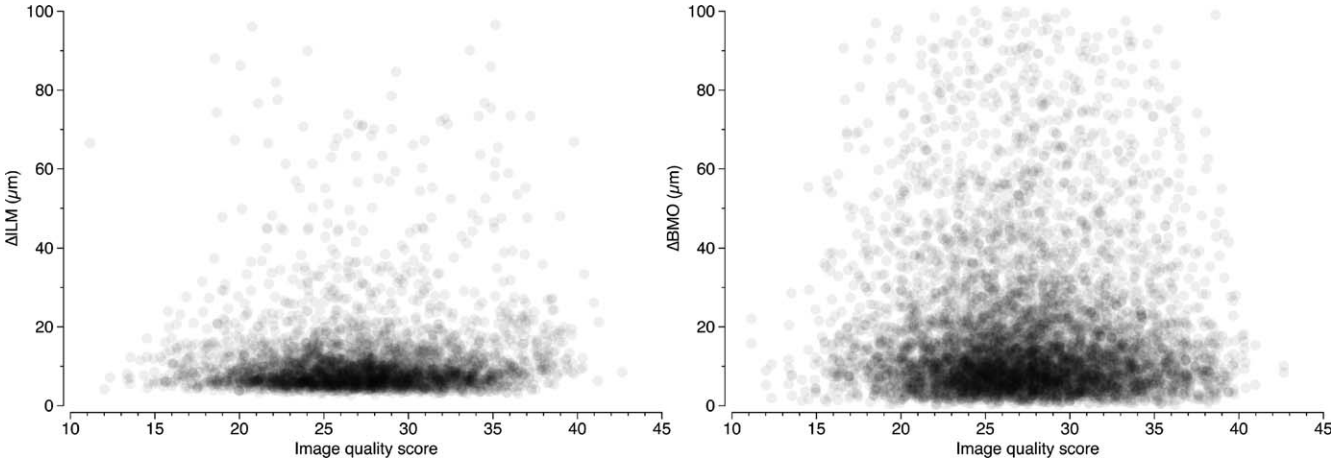

FIGURE 4. Absolute difference between the automated and manual segmentation of the internal limiting membrane (ΔILM, *left*) and Bruch's membrane opening (ΔBMO, *right*) in individual B-scans as a function of image quality score.

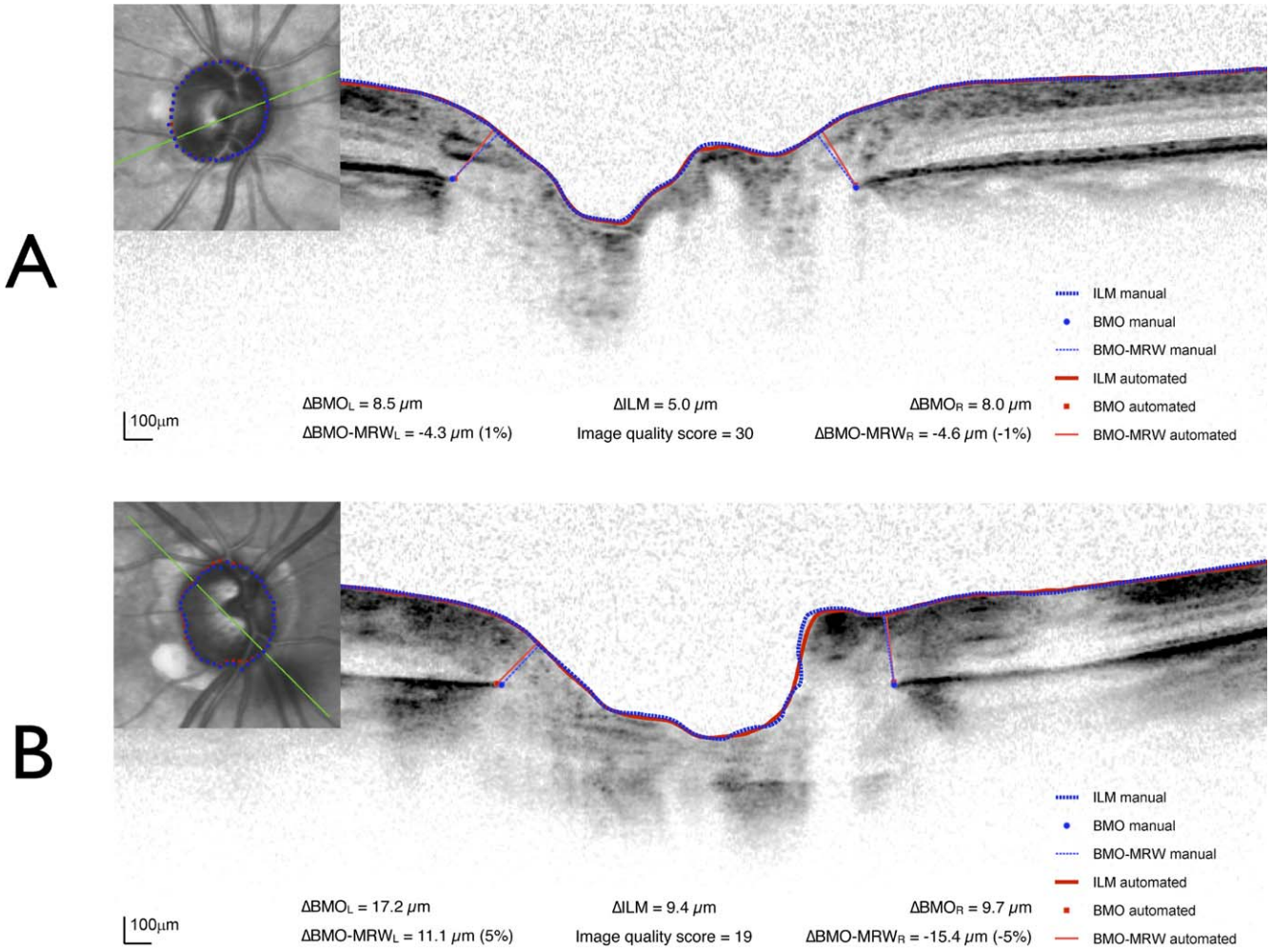

Figure 6. Two examples of B-scans illustrating that image quality score was not a good predictor of the agreement between the automated and manual segmentation methods. (**A**) Image quality in the 71st percentile of the distribution of image quality score and (**B**) in the fourth percentile. *Inset*: Infrared image with BMO segmentation marks shown for the whole optic nerve head and B-scan position (*green line*). *Curves*: ILM. *Lines*: BMO-MRW. *Blue*: Manual segmentation. *Red*: Automated segmentation. Magnitude of differences between the two segmentation methods shown for the *left* (*L*) and *right* (*R*) sides of the B-scan.

the other (Fig. 7B) due to interference from blood vessels. One example of segmentation failure is also illustrated (Fig. 7C).

Discussion

A growing body of research with SD-OCT indicates that neuroretinal rim measurements from BMO correctly reflect the amount of the remaining neuroretinal rim tissue.[5,10–13,23] Accurate automated segmentation of the ILM and BMO is necessary for clinical utilization of these measurements.

Automated segmentation algorithms for SD-OCT have been described; however, their evaluations have been limited to comparisons between the subjectively judged optic disc and cup margins in conventional photographs and the automatically detected BMO and reference plane–based cup measurements in SD-OCT images.[10,16] Recent studies have examined

Table 2. Summary of Subject-Averaged Data*

	Glaucoma	Control	*P*
Image quality score, dB	26.7 (24.0, 29.8)	28.5 (26.0, 29.9)	0.03
ΔILM, μm	10.6 (7.8, 14.4)	7.9 (5.6, 10.9)	<0.01
ΔILM inside BMO, μm	15.8 (10.6, 28.4)	11.9 (8.3, 19.3)	0.02
ΔILM outside BMO, μm	5.7 (4.7, 8.6)	4.5 (4.1, 6.9)	<0.01
ΔBMO, μm	17.4 (13.2, 21.9)	18.9 (14.7, 26.4)	0.09
Absolute ΔBMO-MRW, μm	13.4 (10.6, 16.8)	12.1 (10.0, 16.8)	0.21
Absolute ΔBMO-MRW, %	8.6 (6.1, 14.4)	4.3 (3.1, 5.8)	<0.01
Signed ΔBMO-MRW, μm	−1.7 (−3.8, 3.0)	−2.5 (−5.9, 1.1)	0.33
Signed ΔBMO-MRW, %	−1.0 (−4.0, 1.1)	−0.7 (−2.0, 0.3)	0.18

* Values shown are median (interquartile range).

Investigative Ophthalmology & Visual Science

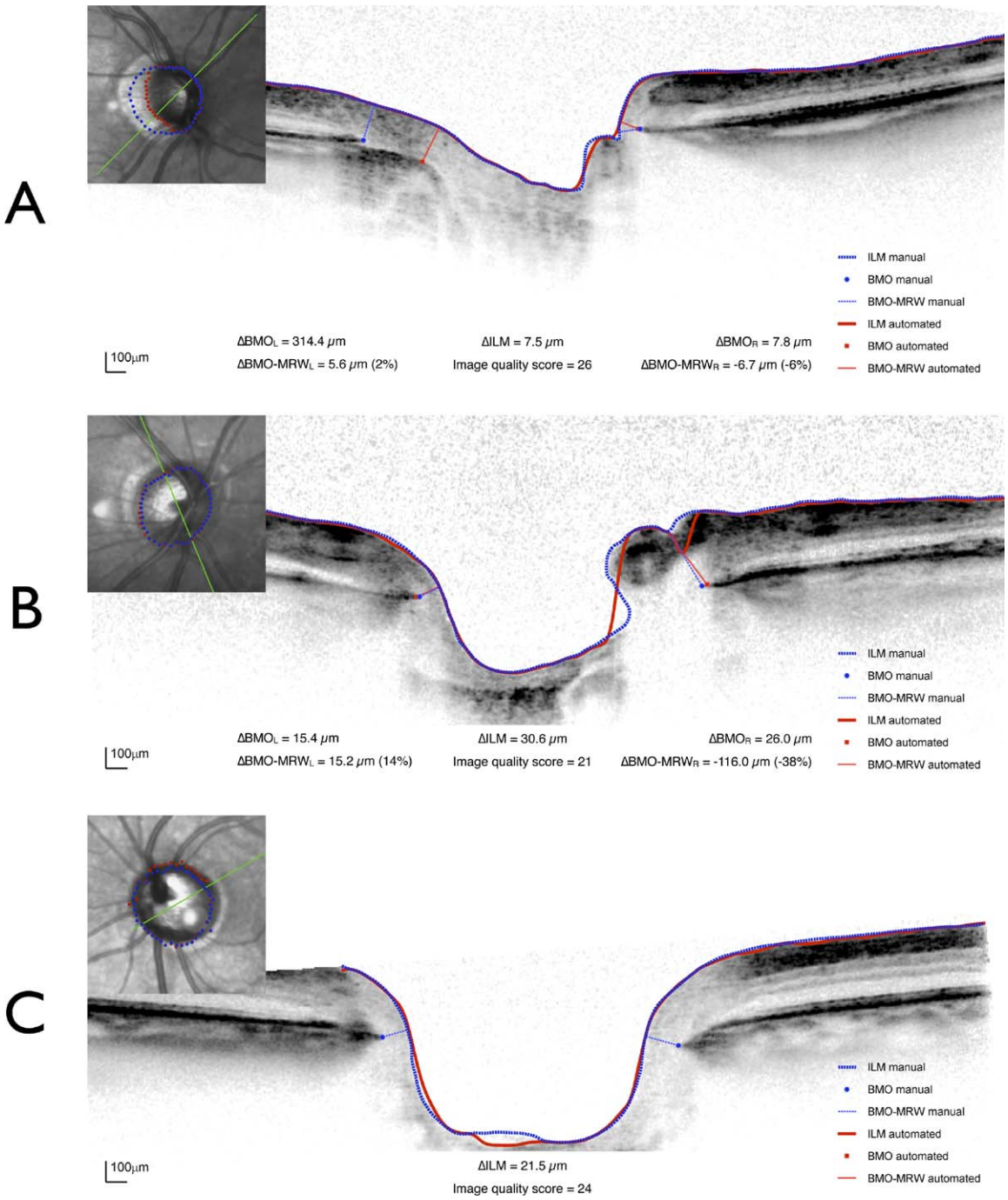

Figure 7. Three examples of B-scans of infrequent but meaningful differences in agreement between the automated and manual segmentation methods. (**A**) Incorrect segmentation of the BMO (*left*) by the automated algorithm on border tissue or sclera. The large difference between the two techniques occurs in the entire temporal optic nerve head (*inset*). (**B**) Influence of a large blood vessel on ILM segmentation, resulting in large differences between the two techniques as well as in BMO-MRW. (**C**) Segmentation failure by the automated technique, likely because of the deep excavation of the optic nerve head. *Curves*: ILM. *Lines*: BMO-MRW. *Blue*: Manual segmentation. *Red*: Automated segmentation. Magnitude of differences between the two segmentation methods shown for the *left* (*L*) and *right* (*R*) sides of the B-scan.

the agreement between automated and manual segmentation in their derivation of disc margin–based measurements such as cup-disc ratio, with the assumption that the termination of the Bruch's membrane/retinal pigment epithelium complex represents the clinical disc margin.[19,20] While these studies have reported generally good agreement between the two methods, the clinically visible optic disc margin seldom corresponds to BMO,[6] making these studies challenging to interpret. In contrast, our evaluation of the automated segmentation algorithm compared automated and manual ILM and BMO segmentation in all of the same B-scan images. We are not aware of previous published studies using the same approach.

The automated segmentation algorithm used in this study yielded a median difference (compared to manual segmentation) of approximately 8 μm in ILM segmentation and approximately 12 μm in BMO segmentation, equivalent to

<2 and <3 image pixels, respectively. However, the distribution of ΔILM and ΔBMO had long positive tails (Fig. 1), with 10% of ΔILM and ΔBMO values being >20 μm and >53 μm, respectively. Hence, while in most cases the automated algorithm provided similar results to manual segmentation, for clinical use, the user should ideally review images for automated segmentation accuracy to identify obvious errors. This verification process is similar to the one required after automated segmentation of the retinal nerve fiber layer. Owing to the complex nature of deep optic nerve head anatomy in which BMO segmentation is affected by factors such as border tissue orientation, overlying blood vessels, and retinal pigment epithelium clumps, it is unlikely that even with further enhancements in automated segmentation, segmentations will not require verification by the user. We did not include glaucoma suspects but assume that the range of ONH appearances across glaucoma patients and controls encompass these subjects. However, if glaucoma suspects systematically differ in ONH structure, then the present results may not be generalizable to them, or indeed to subjects with myopic or other atypical ONH appearances.

With automated segmentation of the ILM and BMO, we wanted to determine whether BMO-MRW, the most important parameter of interest, could be derived reliably (compared to that derived with manual segmentation) without user input. The difference in ΔBMO-MRW between patients and controls was not statistically significant, nor was ΔBMO-MRW related to the severity of disease. Furthermore, the magnitude or direction (positive or negative) of ΔBMO-MRW did not depend on the magnitude of BMO-MRW (Fig. 3). These findings suggest a degree of robustness in the agreement between BMO-MRW values derived from these two segmentation methods. Finally, to place our findings within the context of clinical significance, 95% of all differences in BMO-MRW between the two segmentation methods were, at worst, about 3 times smaller than a conservative estimate of the difference in BMO-MRW between glaucomatous and normal ONHs. Hence, these differences are unlikely to affect even a conservative gauge the discrimination ability of BMO-MRW.

An important limitation of the present study was the lack of a veridical BMO and ILM against which the true error of the automated algorithm can be computed. We assume that lower values of ΔILM and ΔBMO are surrogates of accuracy; however, it is plausible that lower or higher values could result from errors in the manual placement of the segmentation points, especially BMO. It is likely that the true segmentation error for BMO with both methods likely increased as the visibility of BMO decreased. Further research is underway in which the association of ΔBMO with subjectively graded BMO identifiability is examined to test the hypothesis that the automated segmentation algorithm performs worse when the operator also has difficulty with identifying BMO.

It is notable that individual B-scan image quality score was a poor predictor of ΔILM or ΔBMO, suggesting that the segmentation algorithm was robust up to the degree of signal degradation encountered in clinical care. Image quality score explained less than 0.01% and 0.25% of the variability in ΔILM and ΔBMO, respectively. Similarly, mean ΔILM or ΔBMO in individuals did not depend on mean image quality score.

Factors besides image quality had an impact on ΔILM or ΔBMO, hence likely on segmentation accuracy. In externally oblique border tissue configuration,[15,24] where border tissue extends externally from the sclera to fuse with Bruch's membrane, the location of BMO can be mistaken for either border tissue or sclera (Fig. 7). Large differences between the two methods in BMO segmentation can occur in multiple adjacent sections (Fig. 7). Externally oblique border tissue configuration is common in myopic eyes.[25] Because our study excluded subjects with myopia exceeding –6 D, it is probable that ΔBMO and ΔBMO-MRW is higher in that population.

Blood vessels can obscure visibility of the underlying BMO by absorbing incident light and casting shadows. There were no obvious variations in ΔBMO around BMO, except around the superior pole, indicating that the superior vessel trunk was the likely reason for this finding. Blood vessels can also impact automated ILM segmentation, particularly when they are superficial (Fig. 7), as the algorithm can trace the ILM either above or below the vessel depending on the superficiality of the blood vessel. More importantly, ILM segmentation by either method in these cases can have an impact on BMO-MRW if the direction of the minimum rim width is in the vicinity of a blood vessel (Fig. 7). Some efforts to segment blood vessels automatically have been made[26]; however, ultimately, they have to be excluded from calculation of neuroretinal rim tissue. Advances in SD-OCT–based Doppler flowmetry[27] may eventually help to automatically remove the contribution of blood vessels from neural tissue by subtracting the volume generating a Doppler signal.

The contour of the ILM had an impact on ΔILM. Inside BMO, the contour of the ILM has a more complex shape than outside BMO and likely results in a relatively lesser degree of segmentation certainty with both techniques, and probably the reason why ΔILM inside BMO was almost three times higher than outside BMO.

Finally, the scan pattern with which B-scan images are obtained likely affects segmentation accuracy. We used a radial scan pattern centered on the optic nerve head for two reasons: firstly, to ensure that the B-scan had the highest likelihood of intersecting BMO as perpendicularly as possible and reduce the number of candidate positions for BMO; secondly, to have an approximately radially equidistant separation of BMO points to ensure representative sampling. Raster or volume scanning patterns do not intersect BMO perpendicularly (except at the horizontal and vertical poles for horizontal and vertical raster patterns, respectively), hence segmentation accuracy may vary around BMO. Raster patterns also do not yield radially equidistant BMO points. Nonetheless, a comparison of the various scanning patterns may be important in ascertaining the optimal one for segmenting optic nerve head structures with SD-OCT.

In summary, we showed that segmentation of the ILM and BMO with automated and manual methods is highly comparable, with a small number of exceptions. Further input and training from manual segmentations, modification of scan depth according to optic nerve head excavation, and removal of blood vessels from neuroretinal rim calculations are important enhancements that will aid in the incorporation of automated rim measurements into clinical practice.

Acknowledgments

The authors are grateful to Claude Burgoyne, Devers Eye Institute, Portland, Oregon, for providing the segmentation software.

Supported by Grants MOP11357 (BCC) from the Canadian Institutes of Health Research, Ottawa, Ontario; Capes Foundation (ASCR), Ministry of Education of Brazil, Brasilia, Brazil; and equipment and unrestricted research support from Heidelberg Engineering (BCC), Heidelberg, Germany.

Disclosure: **F.A. Almobarak**, None; **N. O'Leary**, None; **A.S.C. Reis**, None; **G.P. Sharpe**, None; **D.M. Hutchison**, None; **M.T. Nicolela**, None; **B.C. Chauhan**, Heidelberg Engineering (F, C, R)

References

1. Srinivasan VJ, Adler DC, Chen Y, et al. Ultrahigh-speed optical coherence tomography for three-dimensional and en face

imaging of the retina and optic nerve head. *Invest Ophthalmol Vis Sci*. 2008;49:5103–5110.

2. van Velthoven ME, Faber DJ, Verbraak FD, van Leeuwen TG, de Smet MD. Recent developments in optical coherence tomography for imaging the retina. *Prog Retin Eye Res*. 2007;26:57–77.
3. Wojtkowski M, Srinivasan V, Fujimoto JG, et al. Three-dimensional retinal imaging with high-speed ultrahigh-resolution optical coherence tomography. *Ophthalmology*. 2005;112:1734–1746.
4. Airaksinen PJ, Tuulonen A, Werner EB. Clinical evaluation of the optic disc and retinal nerve fiber layer. In: Ritch R, Shields MB, Krupin T, eds. *The Glaucomas*. St. Louis, MO: Mosby-Year Book; 1996;617–657.
5. Reis AS, O'Leary N, Yang H, et al. Influence of clinically invisible, but optical coherence tomography detected, optic disc margin anatomy on neuroretinal rim evaluation. *Invest Ophthalmol Vis Sci*. 2012;53:1852–1860.
6. Reis AS, Sharpe GP, Yang H, Nicolela MT, Burgoyne CF, Chauhan BC. Optic disc margin anatomy in patients with glaucoma and normal controls with spectral domain optical coherence tomography. *Ophthalmology*. 2012;119:738–747.
7. Burk RO, Vihanninjoki K, Bartke T, et al. Development of the standard reference plane for the Heidelberg retina tomograph. *Graefes Arch Clin Exp Ophthalmol*. 2000;238:375–384.
8. Mwanza JC, Chang RT, Budenz DL, et al. Reproducibility of peripapillary retinal nerve fiber layer thickness and optic nerve head parameters measured with cirrus HD-OCT in glaucomatous eyes. *Invest Ophthalmol Vis Sci*. 2010;51:5724–5730.
9. Poli A, Strouthidis NG, Ho TA, Garway-Heath DF. Analysis of HRT images: comparison of reference planes. *Invest Ophthalmol Vis Sci*. 2008;49:3970–3975.
10. Abramoff MD, Lee K, Niemeijer M, et al. Automated segmentation of the cup and rim from spectral domain OCT of the optic nerve head. *Invest Ophthalmol Vis Sci*. 2009;50:5778–5784.
11. Chen TC. Spectral domain optical coherence tomography in glaucoma: qualitative and quantitative analysis of the optic nerve head and retinal nerve fiber layer [AOS thesis]. *Trans Am Ophthalmol Soc*. 2009;107:254–281.
12. Povazay B, Hofer B, Hermann B, et al. Minimum distance mapping using three-dimensional optical coherence tomography for glaucoma diagnosis. *J Biomed Opt*. 2007;12:041204.
13. Strouthidis NG, Fortune B, Yang H, Sigal IA, Burgoyne CF. Longitudinal change detected by spectral domain optical coherence tomography in the optic nerve head and peripapillary retina in experimental glaucoma. *Invest Ophthalmol Vis Sci*. 2011;52:1206–1219.
14. Chauhan BC, O'Leary N, Almobarak FA, et al. Enhanced detection of open-angle glaucoma with an anatomically accurate optical coherence tomography-derived neuroretinal rim parameter. *Ophthalmology*. 2013;120:535–543.
15. Strouthidis NG, Yang H, Reynaud JF, et al. Comparison of clinical and spectral domain optical coherence tomography optic disc margin anatomy. *Invest Ophthalmol Vis Sci*. 2009;50:4709–4718.
16. Hu Z, Abramoff MD, Kwon YH, Lee K, Garvin MK. Automated segmentation of neural canal opening and optic cup in 3D spectral optical coherence tomography volumes of the optic nerve head. *Invest Ophthalmol Vis Sci*. 2010;51:5708–5717.
17. Mesiwala NK, Pekmezci M, Huang JY, Porco TC, Lin SC. Comparison of optic disc parameters measured by RTVue-100 FDOCT versus HRT-II. *J Glaucoma*. 2012;21:516–522.
18. Mwanza JC, Oakley JD, Budenz DL, Anderson DR. Ability of cirrus HD-OCT optic nerve head parameters to discriminate normal from glaucomatous eyes. *Ophthalmology*. 2011;118:241–248. e241.
19. Mesiwala NK, Pekmezci M, Porco TC, Lin SC. Optic disc parameters from optovue optical coherence tomography: comparison of manual versus automated disc rim determination. *J Glaucoma*. 2012;21:367–371.
20. Iverson SM, Sehi M. The comparison of manual vs automated disc margin delineation using spectral-domain optical coherence tomography. *Eye (Lond)*. 2013;27:1180–1187.
21. Langenegger SJ, Funk J, Toteberg-Harms M. Reproducibility of retinal nerve fiber layer thickness measurements using the eye tracker and the retest function of Spectralis SD-OCT in glaucomatous and healthy control eyes. *Invest Ophthalmol Vis Sci*. 2011;52:3338–3344.
22. Friedman JH. *SMART User's Guide: Laboratory for Computational Statistics*. Stanford University Technical Report No. 1. 1984.
23. Chauhan BC, Burgoyne CF. From clinical examination of the optic disc to clinical assessment of the optic nerve head: a paradigm change. *Am J Ophthalmol*. 2013;156:218–227. e212.
24. Strouthidis NG, Yang H, Downs JC, Burgoyne CF. Comparison of clinical and three-dimensional histomorphometric optic disc margin anatomy. *Invest Ophthalmol Vis Sci*. 2009;50:2165–2174.
25. Kim M, Kim TW, Weinreb RN, Lee EJ. Differentiation of parapapillary atrophy using spectral-domain optical coherence tomography. *Ophthalmology*. 2013;120:1790–1797.
26. Zhu H, Crabb DP, Schlottmann PG, Ho T, Garway-Heath DF. FloatingCanvas: quantification of 3D retinal structures from spectral-domain optical coherence tomography. *Opt Express*. 2010;18:24595–24610.
27. Werkmeister RM, Dragostinoff N, Palkovits S, et al. Measurement of absolute blood flow velocity and blood flow in the human retina by dual-beam bidirectional Doppler fourier-domain optical coherence tomography. *Invest Ophthalmol Vis Sci*. 2012;53:6062–6071.

Investigative Ophthalmology & Visual Science